Elasto-Static Model and Accuracy Analysis of a Large Deployable Cable-Driven Parallel Robot

Zane Zake, Nicolò Pedemonte, Boris Morinière, Adolfo Suarez Roos, Stéphane Caro

Elasto-Static Model and Accuracy Analysis of a Large Deployable Cable-Driven Parallel Robot*

Zane Zakşe[1][0000−0002−9476−3660], Nicolò Pedemonte[1][0000−0002−4811−3907], Boris Moriniere[2], Adolfo Suarez Roos[1], and Stéphane Caro[3][0000−0002−8736−7870]

[1] IRT Jules Verne, 1 Mail des 20 000 Lieues, 44340, Bouguenais, France
zane.zake@irt-jules-verne.fr
[2] Airbus Operations, rue de l'Aviation, 44340, Bouguenais, France
[3] Nantes Université, École Centrale Nantes, CNRS, LS2N, UMR 6004, 1, rue de la Noe, 44321 Nantes, France
stephane.caro@ls2n.fr

Abstract. Cable-driven parallel robots (CDPRs) have the potential of being the go-to rapidly deployable and reconfigurable robots. This is because cables are used instead of rigid links and thus the overall robot architecture can consist of only four masts, eight motors and very long cables actuating the moving-platform. This paper introduces a large deployable CDPR called ROCASPECT. Its accuracy and repeatability have been evaluated according to ISO 9283:1998. Moreover, the effect of modeling errors and mast compliance on the CDPR accuracy and repeatability is studied.

Keywords: CDPR · deployable · accuracy · repeatability · elasticity

1 Introduction

Cable-driven parallel robots (CDPRs) are a type of parallel robots with cables instead of rigid links. Due to this, CDPRs can have a very large workspace (WS) and a light deployable and reconfigurable structure. However, with the increased size, a decreased accuracy and repeatability can usually be observed. Among the existing large CDPRs we can mention: (*a*) IPANEMA $8\,\mathrm{m} \times 6\,\mathrm{m} \times 5\,\mathrm{m}$ [1]; (*b*) CoGiRo $16\,\mathrm{m} \times 11\,\mathrm{m} \times 6\,\mathrm{m}$ [2]; (*c*) CDPR in the art installation Prince's Tears $20.8\,\mathrm{m} \times 7.3\,\mathrm{m} \times 5.1\,\mathrm{m}$ [3].

To our knowledge only IPANEMA has been evaluated according to ISO 9283:1998 [4] so far. In [1] the pose repeatability of the IPANEMA robot was below 0.75 mm for all tested velocities. Interestingly, the authors observed that the best values could be achieved with the highest velocity of their CDPR. The authors report path repeatability of 0.5 mm. In [5] the pose accuracy is reported to be 37.86 mm. In both papers ground truth measurements were performed

* Supported by IRT Jules Verne (French Institute in Research and Technology in Advanced Manufacturing Technologies for Composite, Metallic and Hybrid Structures).

using a Leica Absolute Laser Tracker AT901-MR (Leica Laser-Tracker) with a certified absolute accuracy of less than 10 µm. For CoGiRo the reported mean accuracy is 50 mm and mean repeatability is 3 mm [6]. However, ISO 9283 relies on the worst accuracy and repeatability measurement instead of the mean. No comparable accuracy or repeatability has been reported for the CDPR used in the art installation.

In this paper, a large deployable CDPR named ROCASPECT, shown in Fig. 1a, is presented. The structure consists of four masts, each being an assembly of multiple pieces, as shown in Fig. 1b. Thus, the CDPR can be stored in a small space when not deployed. The moving-platform (MP) is pulled by 8 cables. In the configuration shown in Fig. 1a, the CDPR size is $23.3\,\mathrm{m} \times 19.0\,\mathrm{m} \times 4.0\,\mathrm{m}$. The MP size is $1.0\,\mathrm{m} \times 1.0\,\mathrm{m} \times 0.5\,\mathrm{m}$ and its mass is 35 kg. The coordinates of cable exit points A_{ij} measured by the Leica Laser-Tracker can be found in Table 1. For security, the masts are fixed to the ground to avoid them tipping over. While the robot footprint is $443\,\mathrm{m}^2$, the actual WS is considerably smaller. Its footprint is computed to be $332.5\,\mathrm{m}^2$ and it is marked with the light green shape in Fig. 2.

During the experiments it was observed that the masts are subject to torsion and bending due to their light structure. In this paper we address the modeling of the CDPR with bending masts as well as the analysis of the effect of mast deformation on the robot accuracy and repeatability.

2 Design and Modeling

As discussed in [3], the height of a CDPR can become a limiting factor as the ground footprint is increased. To counteract the large cable tensions pulling

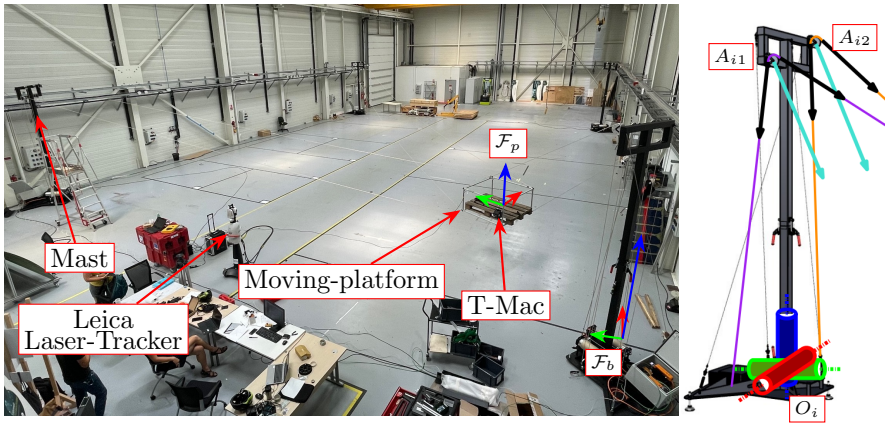

(a) **(b)**

Fig. 1. ROCASPECT: **(a)** test size of $23.3\,\mathrm{m} \times 19.0\,\mathrm{m} \times 4.0\,\mathrm{m}$; **(b)** CAD model of the mast with: two cables (violet and orange); the resultant force of each cable tension (black arrows) on its pulley shown with cyan arrow; mast rotation and torsion shown with one-DoF elastic joints at the bottom of mast

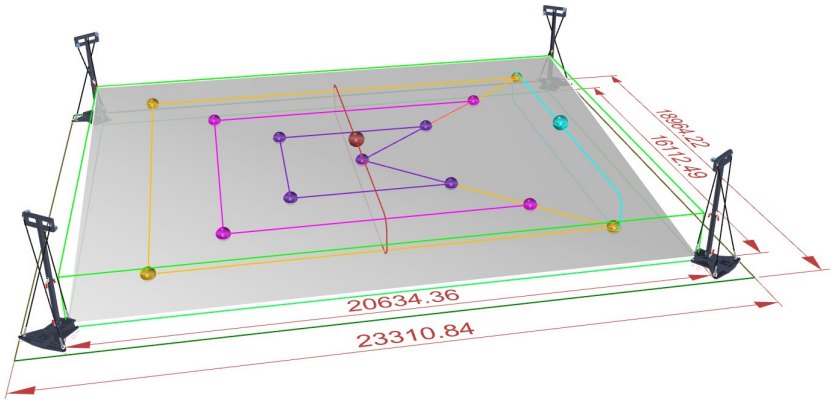

Fig. 2. Schematic of ROCASPECT: (*i*) footprint shown in dark green; (*ii*) WS shown in light green with its diagonal plane in gray; (*iii*) three sets of poses for pose accuracy and repeatability analysis shown in violet, pink and gold; (*iv*) two paths for path accuracy and repeatability analysis shown in brown and cyan

Table 1. Coordinates of ROCASPECT cable exit points

Nominal A_{ij} **in** $\mathcal{F}_b$, m		A^r_{ij} **in** $\mathcal{F}_b$, m		$\|\|\overrightarrow{A_{ij}A^r_{ij}}\|\|_2$, m
A_{11}	$[0.0; 0.0; 3.565]^\top$	A^r_{11}	$[0.057; 0.069; 3.560]^\top$	0.0902
A_{12}	$[-0.772; 0.559; 3.864]^\top$	A^r_{12}	$[-0.699; 0.647; 3.862]^\top$	0.1144
A_{21}	$[-0.765; 16.593; 3.559]^\top$	A^r_{21}	$[-0.705; 16.532; 3.559]^\top$	0.0859
A_{22}	$[-0.006; 17.168; 3.858]^\top$	A^r_{22}	$[0.058; 17.105; 3.854]^\top$	0.0915
A_{31}	$[20.166; 17.135; 3.558]^\top$	A^r_{31}	$[20.117; 17.072; 3.554]^\top$	0.0802
A_{32}	$[20.934; 16.573; 3.867]^\top$	A^r_{32}	$[20.878; 16.500; 3.864]^\top$	0.0912
A_{41}	$[20.926; 0.548; 3.561]^\top$	A^r_{41}	$[20.875; 0.590; 3.562]^\top$	0.0663
A_{42}	$[20.136; 0.0; 3.856]^\top$	A^r_{42}	$[20.094; 0.038; 3.852]^\top$	0.0567

on the masts, ROCASPECT masts are designed with supporting ropes that can be seen in Fig. 1b and Fig. 2. These are certified inelastic Dyneema ropes. However, these ropes have spliced loops on each end and as the splicing tightened during the experiments they elongated by approximately 15 mm or 0.39% of their nominal length of 3.8 m. While the elongation is small and normally would be negligible, it was not possible to tighten the supporting ropes and as a result the masts were bent slightly towards the center of the WS and not as stiff as expected.

After two weeks of experiments the cable exit points were remeasured with the MP positioned at $[10.0; 8.56; 1.0]$. The new measurements, denoted as A^r_{ij} are shown in Table 1 along with the Euclidean distance $||\overrightarrow{A_{ij}A^r_{ij}}||_2$. Furthermore, a certain compliance of masts and as a consequence a displacement of pulleys depending on the MP pose was observed. As an example, the Cartesian coordinates of A_{21} and A_{22} and their distance to A^r_{ij} depending on the MP pose are shown in Table 2.

Table 2. A_{21} and A_{22} measurements depending on the MP position

MP position, m	A_{21}, m	$\delta\mathbf{a}_{21c}$, m	A_{22}, m	$\delta\mathbf{a}_{22c}$, m
$[4.5; 4.5; 1.0]^\top$	$[-0.725; 16.529; 3.555]^\top$	0.0204	$[0.030; 17.090; 3.859]^\top$	0.0322
$[4.5; 12.5; 1.0]^\top$	$[-0.699; 16.524; 3.559]^\top$	0.0103	$[0.063; 17.093; 3.853]^\top$	0.0131
$[15.5; 12.5; 1.0]^\top$	$[-0.689; 16.554; 3.567]^\top$	0.0286	$[0.072; 17.129; 3.847]^\top$	0.0289
$[15.5; 4.5; 1.0]^\top$	$[-0.711; 16.547; 3.561]^\top$	0.0167	$[0.040; 17.119; 3.854]^\top$	0.0232

2.1 Kinematic Model

A CDPR is defined by cable exit points A_{ij} and anchor points B_{ij}, where i denotes the ith mast with $i = 1, \ldots, k$ and $k = 4$; j denotes the jth cable exiting from ith mast with $j = 1, \ldots, p$ and $p = 2$. The ijth cable vector is expressed as:

$$\mathbf{l}_{ij} = {}^b\mathbf{a}_{ij} - {}^b\mathbf{t}_p - {}^b\mathbf{R}_p {}^p\mathbf{b}_{ij} \tag{1}$$

where ${}^b\mathbf{a}_{ij}$ is the Cartesian coordinates vector of A_{ij} expressed in frame $\mathcal{F}_b$; ${}^p\mathbf{b}_{ij}$ is the Cartesian coordinates vector of B_{ij} expressed in frame $\mathcal{F}_p$; ${}^b\mathbf{t}_p$ and ${}^b\mathbf{R}_p$ are the position vector and rotation matrix of the MP expressed in $\mathcal{F}_b$.

The static equilibrium of the MP is given by:

$$\mathbf{W}\boldsymbol{\tau} + \mathbf{w}_g = 0 \tag{2}$$

where $\boldsymbol{\tau}$ is the cable tension vector, $\mathbf{w}_g$ is the MP gravity wrench, and $\mathbf{W}$ is the wrench matrix of the CDPR, defined as [7]:

$$\mathbf{W} = \begin{bmatrix} {}^b\mathbf{u}_{11} & \ldots & {}^b\mathbf{u}_{kp} \\ {}^b\mathbf{R}_p {}^p\mathbf{b}_{11} \times {}^b\mathbf{u}_{11} & \ldots & {}^b\mathbf{R}_p {}^p\mathbf{b}_{kp} \times {}^b\mathbf{u}_{kp} \end{bmatrix} \tag{3}$$

where ${}^b\mathbf{u}_{ij}$ is the unit vector of $\mathbf{l}_{ij}$, namely ${}^b\mathbf{u}_{ij} = \frac{\mathbf{l}_{ij}}{||\mathbf{l}_{ij}||_2}$.

Note that ROCASPECT has large pulleys, thus pulley kinematics must be taken into account, but not detailed here due to the limited space. Please refer to [8–11] for the expression of the unit vector ${}^b\mathbf{u}_{ij}$.

2.2 Mast model

The elongation of the supporting ropes leads to a displacement of cable exit points from A_{ij} to A^*_{ij}, because the mast beam tilts forward at its lower assembly point. Moreover, as the beam and rope assembly (mast) is no longer stiff, applying forces to CDPR cables leads to a small displacement around A^*_{ij}. The latter can be modeled by three perpendicular and intersecting elastic joints at the base of the mast, as shown in Fig. 1b. Although two pulleys are on the same mast, the resulting displacement of each pulley is different and is described as:

$$\delta\mathbf{a}_{ij} = \mathbf{C}_{ij}\mathbf{w}_{ij} \tag{4}$$

where $\mathbf{C}_{ij}$ is the Compliance matrix expressed as:

$$\mathbf{C}_{ij} = \mathbf{J}_{ij}\mathbf{K}^{-1}_{\theta i}\mathbf{J}^\top_{ij} \tag{5}$$

$\mathbf{J}_{ij}$ is the mast Jacobian matrix expressed for each pulley as follows:

$$\mathbf{J}_{ij} = \begin{bmatrix} \mathbf{i} & \mathbf{j} & \mathbf{k} \\ \overrightarrow{A^*_{ij}O_i} \times \mathbf{i} & \overrightarrow{A^*_{ij}O_i} \times \mathbf{j} & \overrightarrow{A^*_{ij}O_i} \times \mathbf{k} \end{bmatrix} \tag{6}$$

with $\mathbf{i}$, $\mathbf{j}$ and $\mathbf{k}$ being the unit vectors along $\mathbf{x}_b$, $\mathbf{y}_b$, and $\mathbf{z}_b$ axes, respectively. The matrix $\mathbf{K}_{\theta i}$ is the (3×3) diagonal joint stiffness matrix of ith mast. $\mathbf{w}_{ij}$ is the resultant wrench exerted on the mast expressed as:

$$\mathbf{w}_{ij} = \begin{bmatrix} \mathbf{f}_i \\ \mathbf{m}_{ij} \end{bmatrix} = \begin{bmatrix} \sum_{z=1}^{p} \mathbf{f}_{iz} \\ \sum_{z=1}^{p} ({}^b\mathbf{a}^*_{iz} - {}^b\mathbf{a}^*_{ij}) \times \mathbf{f}_{iz} \end{bmatrix} \tag{7}$$

with $\mathbf{f}_{ij} = -\tau_{ij}(\mathbf{v}_{ij} + \mathbf{u}_{ij})$, ${}^b\mathbf{a}^*_{ij}$ is the Cartesian coordinates vector of A^*_{ij} expressed in $\mathcal{F}_b$, and $\mathbf{v}_{ij}$ is the unit vector of $\overrightarrow{A^*_{ij}O_i}$. Cable tensions are either measured or estimated, for example by using a tension distribution algorithm [12].

Finally, the actual cable exit point coordinates are thus:

$$A^{\#}_{ij} = A^*_{ij} + \delta\mathbf{a}_{Tij} \tag{8}$$

where $\delta\mathbf{a}_{Tij}$ is the translational part or the last three components of $\delta\mathbf{a}_{ij}$. Note that the cable exit point coordinates A^r_{ij} shown in Table 1 are $A^{\#}_{ij}$ for the MP pose ${}^b\mathbf{t}_p$ =[10.0 m; 8.56 m; 1.0 m; 0°; 0°; 0°].

Mast compliance can be used in the control scheme as shown in Fig. 3.

To find the actual MP pose, given the new cable exit point coordinates, one would need to solve the direct geometric problem defined by (1), which is a complex task. Here, the desired MP pose is used as the first guess and the actual MP pose is found via a least squares algorithm.

Planar case. Let us begin with a planar CDPR with two cables and a point mass MP, as shown in Fig. 4a. Equation (1) becomes $\mathbf{l}_i = \overrightarrow{OA_i} - \overrightarrow{OP_c} = {}^b\mathbf{a}_i - {}^b\mathbf{t}_p$. Similarly, $\mathbf{w}_g = [0,\ -m\mathbf{g}]^\top$ and the wrench matrix (3) becomes $\mathbf{W} = \begin{bmatrix} {}^b\mathbf{u}_1 & {}^b\mathbf{u}_2 \end{bmatrix}$.

Here, each mast has one degree of freedom (DoF) about E_i. A rotation about E_i leads to a displacement of cable exit points from A_i to A^*_i, as shown in Fig. 4b. If the cable lengths l_i remain the same, then the MP is no longer at P_c, but instead at P_*, thus producing a pose error.

For compliant masts, shown in Fig. 4c, cable exit points are at $A^{\#}_i = A^*_i + \delta\mathbf{a}_i$, where $\delta\mathbf{a}_i$ is a small displacement due to mast compliance computed by (4). Of course, in this case mast Jacobian is $\mathbf{J}_i = \begin{bmatrix} h_i\mathbf{E}\mathbf{v}_i \end{bmatrix}$, where h_i is the length of the ith mast, $\mathbf{v}_i$ is a unit vector pointing from E_i to A^*_i and $\mathbf{E} = \left[\begin{smallmatrix} 0 & -1 \\ 1 & 0 \end{smallmatrix}\right]$. Similarly, $\mathbf{w}_{ij}$ is simply $\mathbf{w}_{ij} = \mathbf{f}_i = -\tau_i(\mathbf{v}_i + \mathbf{u}_i)$ using the tensions $\boldsymbol{\tau}$ obtained from (2).

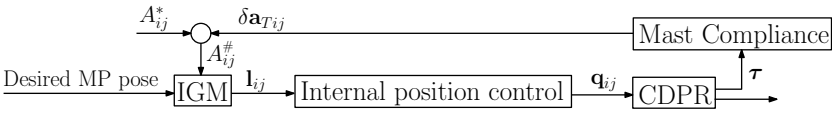

Fig. 3. Control scheme taking into account mast compliance

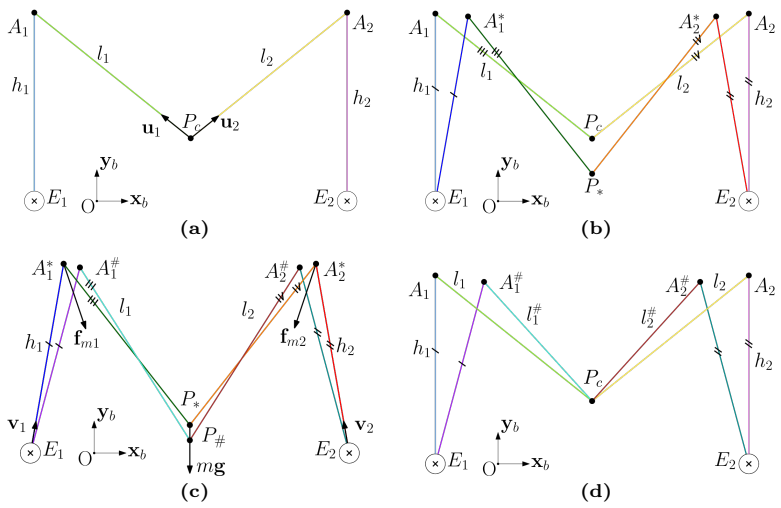

Fig. 4. Planar CDPR **(a)** schematic; **(b)** the desired MP pose does not match with the actual one due to a modeling error; **(c)** forces used to find further mast displacement due to their compliance; **(d)** initialization of the CDPR at a given pose in the presence of modeling errors leads to a difference between actual cable lengths $l_i^{\#}$ and the ones computed by the controller l_i

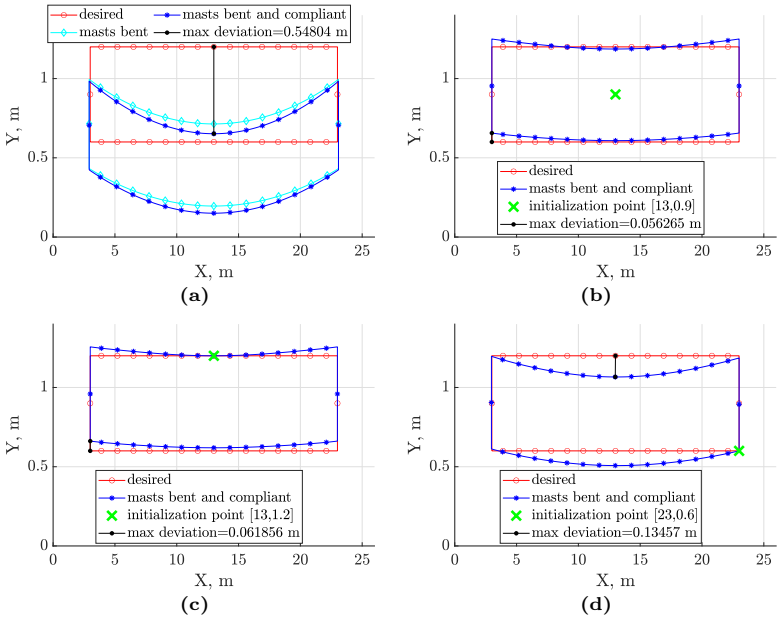

Fig. 5. Trajectory execution **(a)** MP pose computed from cable lengths; **(b)**, **(c)** and **(d)** initializing the robot at different poses with modeling errors

Finally, if the MP is actually at P_c as requested by controller, but the model is not correct, then the actual cable lengths $l_i^{\#}$ will not be equal to cable lengths l_i computed by control, as can be seen in Fig. 4d.

Fig. 5 shows the behavior of a simulated CDPR with compliant masts that is controlled by a controller using the simple CDPR model. Here, the desired trajectory is shown in red and it is executed clockwise from the initial MP pose ${}^b\mathbf{t}_p = [3.0; 0.6]^\top$. Mast height is set to $h_i = 4\,\text{m}$. Masts are rotated by 1.5°, which leads to a distance of approximately 10 cm between A_i and A_i^*. Then, to find $\delta\mathbf{a}_i$ and $A_i^{\#}$, we used $m = 35\,\text{kg}$ and $k_{\theta i} = 710000\,[\text{Nm}]$.

First, if the MP pose is computed from cable lengths, the MP is always significantly lower than desired, as shown in Figs. 4b and 5a. Here, the cyan path corresponds to simulated CDPR with cable exit points at A_i^*, while the blue path corresponds to a simulated CDPR with cable exit points at $A_i^{\#}$.

However, the most likely scenario is shown in Fig. 4d. The initial MP pose is measured by an external system to initialize the controller. The real cable lengths $l_i^{\#}$ are shorter than l_i, which are computed by the controller at the point of initialization. Now the behavior of the robot depends on where the initialization is done, as can be seen in Figs. 5b to 5d. In Fig. 5b, the initialization is in the center of the WS and not on the path. Most of the path, the MP is above the desired pose and the closer it is to the masts, the larger the difference. While the two curves get very close between $X = 8\,\text{m}$ and $X = 12\,\text{m}$, none of the path points match. In Fig. 5c the initialization is done on the path at ${}^b\mathbf{t}_p = [13; 1.2]^\top$ and the rest of the blue path is above the desired one. Finally, in Fig. 5d the initialization is done at ${}^b\mathbf{t}_p = [23; 0.6]^\top$, which leads to the largest deviation compared to Figs. 5b and 5c. Thus, it appears that to minimize the modeling errors, the CDPR should be initialized in the center of the WS or in the center of the path, if it does not coincide with the center of the WS.

3 Accuracy and Repeatability

3.1 ISO Standard 9283:1998

The ISO 9283:1998 [4] describes a collection of experiments to evaluate robot precision. Pose accuracy AP and repeatability RP, as well as path accuracy AT and repeatability RT was assessed. Note that here the notation from the ISO standard is being used. For this, the test plane shown in gray in Fig. 2 was defined. The poses to visit for the evaluation of AP and RP must be placed at the center and at $(0.1 \pm 0.02)d$ from each corner of the test plane, where d is the WS diagonal, $d = 26.238\,\text{m}$. This corresponds to the gold spheres in Fig. 2. However, as it is often shown that CDPRs are more precise at the center of the WS, two additional sets of poses were defined and are shown in pink and violet in Fig. 2. Regarding the choice of the path for AT and RT, we were constrained by our case study, where the main goal was to compare a path in the middle of the WS (shown in brown) and close to WS border (shown in cyan). Furthermore, each path was executed with initialization at the brown sphere and then at the cyan sphere.

3.2 Pose accuracy and repeatability

Each set of five poses was visited 30 times and with several MP velocities defined as a percentage $v_{\%}$ of the maximum velocity of 0.5m/s. Moreover, the violet set was repeated with the remeasured cable exit points A^r_{ij}, shown in Table 1. However, mast compliance was not taken into account during these tests.

Position accuracy and repeatability results can be seen in Fig. 6. First, let us compare the experiments with the nominal CDPR model shown in the first six columns of each bar graph. It can be seen that indeed, the closer the MP to the WS boundaries, the worse the translational accuracy AP, while the components along each global axis do not always follow this trend. On the other hand, the best repeatability is for the largest (gold) test set, while the worst one is for the medium (pink) set. Regarding the rotational accuracy (AP_R) and repeatability (RP_R), in general they both become worse with increased distance from the WS center. However, all the values are very close to one another and the AP_R always remains below 2.5° and RP_R below 0.6°.

It appears that higher velocity leads to better results, as described in [1]. Indeed, both AP and RP are better with $v_{\%} = 100\%$ for the violet and pink test sets compared to $v_{\%} = 10\%$. For the large test set only RP is better.

Comparing the results obtained with the nominal and the remeasured CDPR model, the latter gives a better result, except for AP_z with $v_{\%} = 100\%$. Furthermore, the results for the remeasured model are almost the same no matter the velocity with only two exceptions - the aforementioned AP_z with $v_{\%} = 100\%$, and RP_z with $v_{\%} = 10\%$. Surprisingly, the AP_R and RP_R are worse with the new model, even though they are still very good, not surpassing 1.5° and 0.55°, resp.

Finally, the WS covered in the violet test set is slightly larger than the WS of IPANEMA [1, 5]. With the remeasured model we obtain almost the same accuracy, with the exception of the aforementioned AP_z with $v_{\%} = 100\%$.

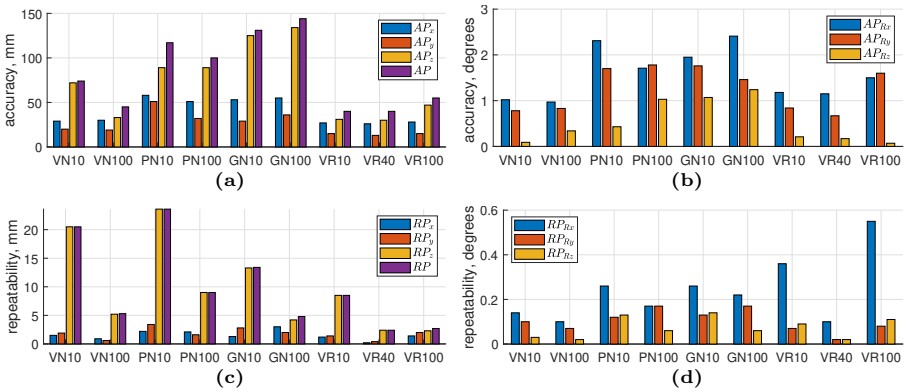

Fig. 6. Pose accuracy AP and repeatability RP. Notation: first letters *V*, *P*, *G* refer to violet, pink and gold sets of poses shown in Fig. 2, resp.; second letters *N* and *R* refer to the use of nominal or remeasured CDPR models shown in Table 1; numbers *10*, *40*, *100* refer to velocity as percentage of max MP velocity of 0.5 m/s

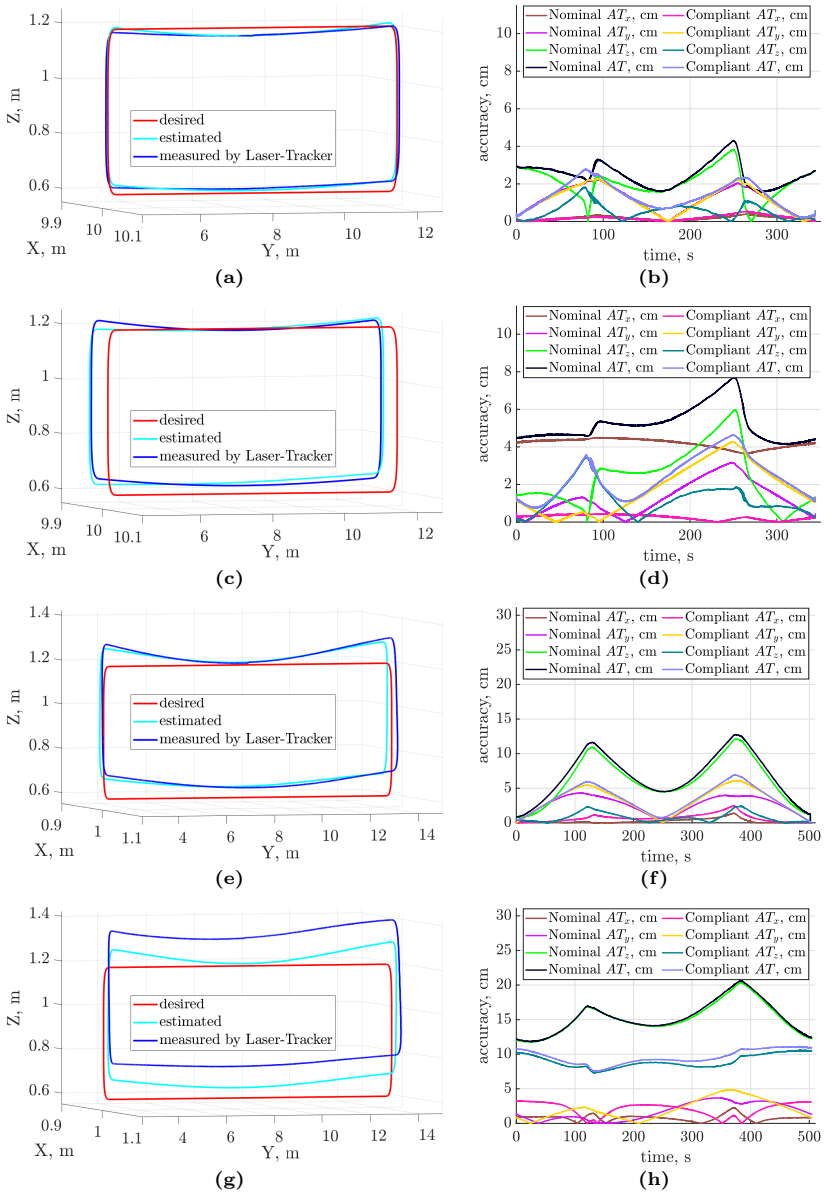

Fig. 7. Path and accuracy: **(a)** and **(b)** path and initialization in the middle of the WS; **(c)** and **(d)** path in the middle of the WS, but initialization on the side; **(e)** and **(f)** path and initialization on the side of the WS; and **(g)** and **(h)** trajectory on the side of the WS, but initialization in the middle

3.3 Path accuracy and repeatability

As explained in Section 3.1 and shown in Fig. 2, two paths parallel to the global ZY plane were selected: one in the center and one on the side of the WS. More-

over, two initialization poses were used for each path: in the center and on the side of the WS. The starting position is $[10.0; 8.56; 1.2]$ or $[1.0; 8.56; 1.2]$, corresponding to the brown and cyan spheres shown in Fig. 2, resp.

The results are shown in Fig. 7 on the left, where the desired path is shown in red and the executed one is shown in blue. Furthermore, the evolution of the translational accuracy AT along the path can also be seen in Fig. 7 on the right with the notation *nominal*. Here, the translational accuracy is the difference between the desired path and the measured one. It is clear that the best behavior is when both the path and the initialization are in the center of the WS, shown in Figs. 7a and 7b. Accuracy AT is 2.5 cm on average, and the worst peak of 4.6 cm is due to AT_z. Note that the shape of the executed trajectory is very close to the simulated one in Fig. 5b. Then, if the initialization is done on the side of the WS (Fig. 7c), the average AT is 5.2 cm, while the peak reaches 7.7 cm, thus roughly doubling when compared to Figs. 7a and 7b. The main reason behind this increase is a considerable increase of AT_x, that remains at about 4 cm throughout the path. Thus, it is important to initialize the robot on the trajectory to have the best accuracy.

Next, in Fig. 7e both the initialization and the path are on the side of the WS. The executed trajectory is even less precise and is very similar to the simulated one in Fig. 5c. As initialization is done on the path, the AT_x is small. However, the large deviation along Z drives AT to peak at 12.8 cm. Finally, in Fig. 7g the initialization is now done in the center, while the path is on the side of the WS. This leads to the worst accuracy out of the four scenarios, AT peaking at 20.6 cm due AT_z. Thus, in both scenarios shown in Figs. 7c and 7g initialization far from the path leads to worse accuracy.

3.4 Accuracy and repeatability with the compliant mast model

In this section the model proposed in Section 2.2 is verified by estimating the behavior of ROCASPECT given the desired paths shown in red in Fig. 7. It is assumed that the final cable exit points $A_{ij}^{\#}$ are computed as $A_{ij}^{\#} = A_{ij}^{*} + \delta\mathbf{a}_{ij}$, where A_{ij}^{*} corresponds to cable exit point coordinates after the elongation of supporting ropes by 1.5 cm and $\delta\mathbf{a}_{ij}$ is the additional cable exit point displacement due to mast compliance. To compute $\delta\mathbf{a}_{ij}$, the stiffness matrix of each mast is set so that the diagonal components are $k_{11} = 200000\,[\text{Nm}]$, $k_{22} = 500000\,[\text{Nm}]$, $k_{33} = 300000\,[\text{Nm}]$. These stiffness coefficients were obtained by simulating the robot with the MP poses given in Table 2 and tuning the coefficients to get similar cable exit point coordinates. Cable tensions $\boldsymbol{\tau}$ are also needed, however the real cable tensions were not measured. Accordingly, the cable tensions were estimated by using the tension distribution algorithm described in [13, 14].

The resulting paths are shown in cyan in Fig. 7 on the left. The translational accuracy AT is plotted in Fig. 7 on the right with the notation *Compliant*. Here AT is the difference between the estimated and the measured paths. Right away it can be seen in Fig. 7a that the estimated and measured paths are almost the same. Compliant AT_x and AT_y almost coincide with the nominal ones in Fig. 7b, while AT_z is considerably lower. Indeed, now AT peaks at 2.8 cm due

Table 3. MP translational errors with the nominal and the compliant models

Path	**Initialization**	NAT_{max}, mm	NAT_{avg}, mm	CAT_{max}, mm	CAT_{avg}, mm
Center	Center	43.1	24.8	28.0	13.6
Center	Side	77.1	52.0	46.3	24.0
Side	Side	127.6	67.8	69.2	34.2
Side	Center	206.3	154.0	111.4	95.7

to AT_y. Thus, while the compliant model is indeed considerably closer to the real robot, there are some sources of errors, affecting AT_y that are not modeled. In Fig. 7c, the difference between the cyan and blue paths is a bit larger, but they are still very similar. As can be seen in Fig. 7d, compliant AT_x is almost 0, thus the error of the nominal AT_x comes mainly from the difference between the control model A_{ij} and the compliant model $A^{\#}_{ij}$. Compliant AT_z is also smaller than the nominal one, consequently compliant AT averages at 2.4 cm and peaks at 4.6 cm, which is almost twice better than the nominal AT.

In Figs. 7e and 7f, thanks to the dramatic decrease of compliant AT_z to less than 3 cm, the accuracy AT is now twice better than the nominal one. Finally, the difference between the estimated and the measured paths is large in Fig. 7g. Indeed, the compliant AT_z remains at about 10 cm, as shown in Fig. 7h, however even that is significantly better than the nominal AT_z that averages at 15.4 cm and peaks at 20.6 cm. This is also the only case where a large difference between nominal and compliant AT_x can be seen. It seems that initializing the MP in the center and then working on the side of the WS accentuates the modeling issues.

4 Conclusions

In this paper the accuracy and repeatability of a very large deployable CDPR measured according to the ISO 9283:1988 standard is presented. A simple compliant mast model is then proposed to explain the behavior observed during experimentation.

Overall, the results are comparable to the state of the art, especially with the remeasured model: about 5 cm for accuracy and less than 1 cm for repeatability, which is 0.19% and 0.04% of the WS diagonal, resp. However, to obtain this model, it is important to first have a working-in period for a CDPR to ensure that all cables (supporting and actuated) stretch and tighten in their knots, splices or winding systems.

CDPR accuracy depends on the distance of the MP to its WS center, as could be seen in both sets of experiments. Moreover, as shown in the path experiments, the initialization pose matters as well. Indeed, a badly chosen initialization pose can accentuate the differences between the model and the actual robot.

CDPR accuracy depends also on the robot model used within the controller. Indeed, if the model is not correct or too simple, the behavior of the robot cannot be precise. Using a compliant mast model the obtained behavior is very similar

to the measured one given the same control output. Note that our estimation was obtained without the real tension measurements, without a mast stiffness identification and assuming that all masts have the same stiffness coefficients. Thus, the resulting accuracy can be significantly improved by using the proposed model in the controller. As a consequence, future work includes mast stiffness identification and implementation of a control scheme that takes into account cable tensions and mast compliance.

References

1. A. Pott, H. Mütherich, W. Kraus, V. Schmidt, P. Miermeister, A. Verl, "IPAnema: a family of cable-driven parallel robots for industrial applications", in: *Cable-Driven Parallel Robots (CableCon)*, pp. 119–134, Springer, Berlin, Heidelberg, 2013.
2. T. Dallej, M. Gouttefarde, N. Andreff, R. Dahmouche, P. Martinet, "Vision-based Modeling and Control of Large-Dimension Cable-Driven Parallel Robots", in: *Intelligent Robots and Systems (IROS)*, pp. 1581–1586, IEEE, Vilamoura, Algarve, Portugal, 2012.
3. J.-P. Merlet, Y. Papegay, A.-V. Gasc, "The Prince's tears, a large cable-driven parallel robot for an artistic exhibition", in: *International Conference on Robotics and Automation (ICRA)*, pp. 10378–10383, IEEE, Paris, France, 2020.
4. ISO 9283:1998. "Manipulating industrial robots – Performance criteria and related test methods."
5. V. Schmidt, A. Pott, "Implementing extended kinematics of a cable-driven parallel robot in real-time", in: *Cable-Driven Parallel Robots (CableCon)*, pp. 287–298, Springer, Berlin, Heidelberg, 2013.
6. V. Auffray, "Vers la manipulation précise de grandes pièces dans de très grands espaces de travail", `https://www.cnrs.fr/mi/IMG/pdf/cable_tecnalia_cnrs.pdf`
7. A. Pott, *Cable-Driven Parallel Robots: Theory and Application*, pp. 52–56, vol. 120., Springer, 2018.
8. A. Pott, "Influence of pulley kinematics on cable-driven parallel robots", in: *Latest Advances in Robot Kinematics*, pp 197–204, Springer, Dordrecht, 2012.
9. E. Picard, S. Caro, F. Claveau, F. Plestan, "Pulleys and Force Sensors Influence on Payload Estimation of Cable-Driven Parallel Robots", in: *Intelligent Robots and Systems (IROS)*, pp. 1429–1436, IEEE, Madrid, Spain, 2018.
10. T. Paty, N. Binaud, S. Caro, S. Segonds, "Cable-Driven Parallel Robot Modelling Considering Pulley Kinematics and Cable Elasticity", in: *Mechanism and Machine Theory*, article 104263, vol. 159, 2021.
11. Z. Zake, "Design and stability analysis of visual servoing on cable-driven parallel robots for accuracy improvement", PhD thesis, École Centrale de Nantes, 2021.
12. E. Picard, S. Caro, F. Plestan, F. Claveau, "Stiffness Oriented Tension Distribution Algorithm for Cable-Driven Parallel Robots", in: *Advances in Robot Kinematics (ARK)*, pp. 209–217, Springer, Cham, 2020.
13. L. Mikelsons, T. Bruckmann, M. Hiller and D. Schramm, "A real-time capable force calculation algorithm for redundant tendon-based parallel manipulators", in: *International Conference on Robotics and Automation (ICRA)*, pp. 3869–3874, IEEE, Pasadena, CA, USA, 2008.
14. T. Rasheed, P. Long, D. Marquez-Gamez, S. Caro, "Tension Distribution Algorithm for Planar Mobile Cable-Driven Parallel Robots", in: *Cable-Driven Parallel Robots (CableCon)*, pp. 268-279, Québec, Canada, 2017.